Dawsonite and ankerite formation in the LDX-1 structure, Yinggehai basin, South China sea: An analogy for carbon mineralization in subsurface sandstone aquifers

Lei Yu, Keqiang Wu, Li Liu, Na Liu, Xiaoran Ming, Eric H Oelkers

Dawsonite and ankerite formation in the LDX-1 structure, Yinggehai basin, South China Sea: An analogy for carbon mineralization in subsurface sandstone aquifers

Lei Yu[a, b], Keqiang Wu[c], Li Liu[a, *], Na Liu[a], Xiaoran Ming[d], Eric H. Oelkers[b, e, *]

a. College of Earth Sciences, Jilin University, 130061 Changchun, PR China

b. Department of Earth Sciences, University College London, Gower Street, WC1E 6BT London, United Kingdom

c. China National Offshore Oil Corporation (CNOOC) Research Institute, 100028 Beijing, China

d. The First Monitoring and Application Center, China Earthquake Administration, Tianjin, 300180, China

e. GET-Université de Toulouse-CNRS-IRD-OMP, 14 Avenue Edouard Belin, 31400 Toulouse, France

Abstract

The geochemistry and petrology of the LDX-1 structure of the Yinggehai basin, a natural analog of a sedimentary carbon storage site, was investigated to understand the consequences of the charging of CO_2 gas in this system. The rocks in this structure are dominated by subarkose and sublitharenite sandstones. The authigenic minerals formed after CO_2 injection are dawsonite, microcrystalline quartz, kaolinite and ankerite. Dawsonite and ankerite are formed just beneath a CO_2 bearing anticlinal structure due to the reactions between silicate minerals (feldspars and clay minerals) and the fluid phase. Carbon and oxygen isotopic analyses indicate that the main carbon source for dawsonite and ankerite formation was mantle magmatic CO_2. The aqueous activities of sodium and calcium, the partial pressure of CO_2, pH and temperature are the key factors influencing the stability of the dawsonite and ankerite. The presence of the anticlinal structure maintaining a locally high CO_2 partial pressure in the waters beneath this structure is likely responsible for the observed long-term persistence of dawsonite and ankerite in this system.

Keywords: authigenic carbonate minerals, carbon and oxygen isotopes, dawsonite stability, carbon capture and storage (CCS), Yinggehai Basin

1 Introduction

Carbon-dioxide emissions to the atmosphere by anthropogenic industrial activities are a key factor causing global climate change (IPCC, 2005, 2007; Manabe and Stouffer, 1993). The injection of anthropogenic CO_2 into deep geologic formations has been advocated to slow increasing atmospheric CO_2 concentrations and its effect on global climate (Bachu et al., 1994; Bachu, 2003; IPCC, 2005, 2007; Oelkers and Cole, 2008). There are four mechanisms of carbon storage in the subsurface: structural and stratigraphic trapping, residual CO_2 trapping, solubility trapping and mineral trapping (IPCC, 2005; Johnson et al., 2001). Of these, mineral trapping, and in particular in-situ carbon mineralization, is the most stable and safe carbon storage solution (Lackner et al 1995; Johnson et al., 2001; Matter et al., 2016; Oelkers et al., 2008; Power et al. 2013).

Sandstone aquifers with impermeable cap-rocks are commonly considered for carbon storage as they are have adequate permeability and pore space, and are abundant in the subsurface (Benson and Cole, 2008; IPCC, 2005; Xu et al., 2005). A number of studies have shown that calcite, siderite, magnesite, dolomite, ankerite and dawsonite could form in various sandstones in response to CO_2 injection. (Baker et al., 1995; Fischer et al., 2010; Gao et al., 2009; Gaus et al., 2005; Hellevang et al., 2013; Higgs et al., 2013, 2015; Hitchon, 1996; Klajmon et al., 2017; Liu et al., 2011; Moore et al., 2005; Pauwels et al., 2007; Pearce et al., 2016; Pham et al., 2011; Uysal et al., 2011; Van Pham et al., 2012; Worden, 2006; Xu et al., 2004, 2005, 2007, 2010; Yu et al., 2015; Zhao et al., 2018; Zhou et al., 2014). Of these minerals, dawsonite ($NaAl(OH)_2CO_3$) is particularly attractive as a carbon storage host as it contains sodium and aluminum, which can be abundant in sedimentary silicates. This mineral, however, is more reactive and less stable than many of the aforementioned divalent

metal carbonate minerals (Bénézeth et al., 2007; Hellevang et al., 2005, 2011).

The LDX-1 structure in the Yinggehai basin of South China Sea provides an insightful analogy for the study of mineral carbonation in sandstone aquifers (Fig. 1). The gas phase in the LDX-1 structure contains as much as 93 volume percent CO_2 and this CO_2 has a distinct inorganic carbon isotopic signature (He et al., 2005; Huang et al., 2003). In addition, past studies concluded that the CO_2 gas injection into this structure occurred after that of the hydrocarbon gases (Huang et al., 2004; Sun and Wang, 2000), which is similar to scenerios that might be encountered by injecting into former oil field reserviors.

The purpose of this study is to characterize the mineralogy and paragenesis in two wells drilled into the LDX structure to investigate sandstone diagenesis and carbonate mineral formation in response to the influx of CO_2. Results will be used to gain further insight into the potential for mineral carbonation in sedimentary sandstones as part of subsurface carbon storage efforts.

2 Geological setting

The Yinggehai basin, which developed during the Cenozoic, is a natural gas-rich rift basin. It is located between the Indian and South China plate, formed by the combination of lithosphere extension and the deep, strike-slip Red River fault. The direction of this basin is Northwest-Southeast, with a total area of approximately 11×10^4 km^2 (Huang et al., 2009; Wan et al., 2007; Fig. 1a, b). Two northwest-trending, deep-to-basement faults divide the Yinggehai basin into three sub-structural units: The Central Depression, the Ying Dong Slope and the Ying Xi Slope (see Fig 1). The central depression consists of two tectonic units: the Lin Gao uplift and the diapir structure belt (Fig 1b; Zhu et al., 2004). During the Miocene, the Yinggehai basin was filled with argillaceous sediments along the fault and formed a series of diapir structures in the central depression zone (Huang et al., 2009). He et al. (2005) reported that most of the natural gas reservoirs with high CO_2 contents are concentrated in these diapir

structures.

The basement of the Yinggehai basin is dominated by palaeozoic magmatic rocks (Hao et al., 1998). According to the drilling strata, the Cenozoic sediments include the Eocene Lingtou Formation, the Oligocene Yacheng and Lingshui Formations, the Miocene Sanya, Meishan, and Huangliu Formations, the Pliocene Yinggehai Formation and the Quaternary Ledong Formation. The thickness of the Cenozoic sediments in this basin is up to 16-17 km (Gong et al., 1997; Huang et al., 2004, 2009; Meng et al., 2012; Zhu et al., 2007) (Fig. 2). The Lingtou Formation mainly consists of sandstone and mudstone. The Yacheng and Lingshui Formations are composed of mudstone and silty mudstone interbeded with mudstone. Both the Sanya and Meishan Formations are dominated by calcareous mudstone. The Huangliu, Yinggehai and Ledong Formations are mainly siltstone, sandstone and interbedded mudstone. The Miocene mudstone is the main source rock of natural gas in this basin, while the interbedded mudstone and sandstone of the overlying Huangliu and Yinggehai Formations provide a good reservoir and cap rock system for the basin (Wang and Huang, 2008). According to the logging data, the Yinggehai and Huangliu formations contain the main CO_2 gas reservoirs in the basin.

The LDX-1 Structure is a dome structure located in the southeast of the Ledong area in the central depression of the Yinggehai Basin (Fig. 1b). The gas reservoir in the LDX-1 structure is an anticline formed by a mud diapir. The rocks containing the CO_2–rich gas reservoirs consist mainly of the marine sandstones of the Pliocene Yangehai Formation (Fig. 2) and are located at a depth of 392 m to 2300 m (Huang et al., 2004; Li et al., 2005). According to gas measurements, the LDX-1 reservoirs are dominated by hydrocarbon gas and CO_2; the CO_2 content ranges from 41.9% to 78.7% (Huang et al., 2004).

There were two major episodes of gas emplacement into the Yinggehai basin, the first from an organic source and dominated by CH_4 and the second from an inorganic sourced and dominated by CO_2. According to the Xie et al., (2014), the arrival of the

CH_4 dominated gas was at approximately 3.7 Ma. The CO_2 dominated gas arrived later. Estimates of its arrival time range from 0.3 to 1.9 Ma (Fu et al., 2016; Huang et al., 2005; Wang et al., 2004; Xie et al., 2014). As such this basin provides a close natural analogue to the filling of a former hydrocarbon reservoir with CO_2 as part of subsurface carbon storage efforts.

3 Sampling and research methods

A total 159 sandstone samples were collected from the gas reservoir layers of the LDX-1 structure of the Yinggehai Formation. The samples were collected from the depths of 1841.62 to 1869.02 m (from well LDX-1-1) and of 1958.07 to 1905.13 m (from well LDX-1-4). The compositions of the sandstone samples were determined by counting 300 points in each thin section following the approach of Dickson (1965) using an OLYMPUS BX51 polarizing microscope. To identify the carbonate minerals, all the thin sections were stained with Alizarin Red S and K-ferricyanide solutions following the procedure of Dickson (1965). Authigenic mineral observations and energy spectrum analyses were performed at the Research Center of Paleontology and Stratigraphy of Jilin University, using a JEOL JSM-6700F scanning electron microscope (SEM), equipped with energy dispersive X-ray spectrometer (EDS) analyzer manufactured by Oxford, UK; mineral surfaces were gold coated prior to this analysis.

Based on a systematic petrographic study of the sandstone in the gas reservoirs, 10 dawsonite-bearing samples were selected for carbon and oxygen isotope analyses using MAT253 isotopic ratio mass spectrometers at the Analytical Laboratory of The China National Nuclear Corporation (CNNC) Beijing Research Institute of Uranium Geology. The analytical method for obtaining stable isotopic compositions is based on past studies such as Liu et al. (2011). Samples were grounded into a powder using an agate mortar and pestle. The ground powers were sieved and the > 74 μm fraction was collected, then dried for 2 h at 105 ºC under atmospheric pressure, to remove potential

surface volatile phases, before analyzing. For carbon and oxygen isotope analyses, 99% phosphoric acid (produced by Merck KGaA, Darmstadt, Germany) was reacted with crushed whole rock powders at 25 ºC or 50 ºC (McCrea, 1950). For dawsonite analysis, CO_2 released from samples during the first 4 h reactions at 25 ºC was discarded, as this gas likely originated from the decomposition of calcite. After that, the reaction was continued for another 24h and the CO_2 was collected for the analysis of dawsonite isotopic compositions (Becker, 1971; Rosenbaum and Sheppard, 1986; Sharma and Clayton, 1965). For ankerite analysis, the CO_2 released during the first 24 h reaction at 25 ºC was discarded, as it likely originated from calcite and dawsonite decomposition, then the reaction temperature was raised to 50 ºC followed by the collection of the CO_2 produced by the decomposition reaction during subsequent 48 h (Uysal et al., 2011). The precision of the analyses is ±0.1‰ for $\delta^{13}C$ and ±0.2‰ for $\delta^{18}O$. All reported isotope values in this study are relative to the Belemnitella americana from the Peedee Formation (PDB) standard for carbon and Standard Mean Ocean Water (SMOW) for oxygen.

All the speciation and solubility calculations were conducted using PHREEQC v. 3 (Parkhurst and Appelo, 2013) with its Lawrence Livermore National Laboratory (LLNL) thermodynamic database after adding to it the stability constant for ankerite. The stability of ankerite in this study is based on the formula ($Ca(Fe_{0.5}Mg_{0.5})(CO_3)_2$) (see below). Its thermodynamic properties were estimated from the stoichiometrically weighted sum of the calcite, siderite and magnesite stability constants (Xu et al., 2004). The thermodynamic properties required for this estimate were calculated using the SUPCRTBL database (Zimmer et al., 2016). The resulting ankerite equilibrium constant and enthalpy of reaction are 0.642 and -69.326 kJ/mol at 70 °C and -0.087 and -77.803 kJ/mol 100 °C. Thermodynamic properties in the LLNL database are consistent with those of dawsonite reported by Bénézeth et al. (2007). The Truesdell-Jones equation was used to calculate aqueous activity coefficients and the fugacity for CO_2 gas was calculated using the ThermoSolver 1.0 software (Barnes,

2006).

4 Results

4.1 Petrographic characteristics

The dawsonite in the LDX-1 structure is hosted in fine-grained subarkose and lithic quartz sandstones. The observed detrital minerals are mainly quartz (16.7% to 64.7%), feldspar (up to 12.0%) and rock fragments (up to 23.0%). The modal compositions of the detrital minerals are shown schematically in Fig 3. The feldspar is mainly comprised of plagioclase and also contains small amounts of orthoclase and perthite. The rock fragments mainly consist of metamorphic debris (up to 19%), granite debris (up to 8%), and sedimentary debris (up to 7%).

4.2 Authigenic mineralogy and paragenesis

The authigenic minerals observed in the rock samples are dawsonite, quartz, siderite, dolomite, ankerite, mixed-layer clays consisting of illite and smectite, and kaolinite.

4.2.1 Dawsonite

Dawsonite is principally found at depths of 1841.27 to 1867.23 m in well LDX-1-1 and 1863 to 2018 m in well LDX-1-4 with its content ranging from 0.2 to 6 Vol% as determined by point counting (see above). Dawsonite aggregates nucleate as microcrystalline grains then grow radially outward into the sandstone pores. Dawsonite growth usually terminates at the edge of the detrital minerals (eg. quartz and feldspar). Dawsonite could also be observed growing on dolomite (Fig. 4a, b), potassium feldspar and plagioclase (Fig 4c, d). The EDS results show that the dawsonite mainly consists of carbon, oxygen, sodium and aluminum having weight percents of 7.25 to 22.23, 50.43 to 66.93, 3.58 to 14.69, and 7.27 to 30.26 respectively (see Table 1).

197

198 *4.2.2 Authigenic quartz*

199 Two kinds of authigenic quartz were observed: quartz overgrowths and
200 microcrystalline quartz. The content of authigenic quartz is low, generally less than
201 0.5%. Quartz overgrowths are the among the earliest authigenic silicate minerals
202 observed and are evident due to clay rims between detrital quartz and these
203 overgrowths. The thickness of the quartz overgrowths ranges from 0.01 to 0.06 mm.
204 Furthermore, we observed some radial dawsonite surrounded by quartz overgrowths
205 (see Fig. 4e), suggesting some of the quartz precipitated concurrently with or after the
206 dawsonite. In addition, SEM images show that the microcrystalline quartz was
207 distributed in sandstone pores sporadically and is associated with kaolinite. This
208 kaolinite is also associated with dawsonite in some places (Fig. 4f). Such observations
209 further suggest that the microcrystalline quartz formed during same time period as the
210 dawsonite.

211

212 *4.2.3 Siderite*

213 Most siderite was distributed in pores as subhedral intergranular crystals or
214 aggregates along the boundaries of the detrital grains (Fig. 4g). The content of the
215 siderite ranges from 0.5% to 13.5% in the bulk rock and the crystal sizes range from
216 0.01 mm to 0.03 mm. The color of the siderite is yellow brown to dark brown under
217 single polarized light. The siderite crystals were distributed either in the inner side of
218 quartz overgrowth or near the clay rims surrounding the original quartz grain
219 boundaries, indicating that siderite formation was earlier than or concurrent with the
220 quartz overgrowths.

221

222 *4.2.4 Dolomite*

223 The dolomite content (0.5 to 43 Vol%) varied substantially in the studied cores. As
224 dolomite is not stained by Alizarin Red S and K-ferricyanide solutions, it is readily

distinguished from other carbonates. Under the polarizing microscope, some dolomite was observed being replaced by dawsonite aggregates (Fig. 4h). SEM analysis revealed that the ends of some needle-like dawsonite crystals terminate at the faces of dolomite crystals exhibiting a “bridged phenomenon" (Figure 4a, b). Both sets of observations imply that the dolomite formed earlier than the dawsonite, yet the presence of some detrital dolomite cannot be discounted.

4.2.5 Ankerite

Ankerite (0.5 to 36 Vol%) mainly surrounds dolomite crystals as rim-like growths (Fig. 4i) or as euhedral to subhedral intergranular crystals (Fig. 4j, k). Under the Back Scattered Electron (BSE) mode, the ankerite is seen to form of nearly equal ring-like shapes along the dolomite surfaces as it replaced this mineral. Some ankerite is seen to have grown on dawsonite (Fig 4j, k). Such observations suggest that ankerite formation occurred later than both the dolomite and dawsonite. EDS analyses results for ankerite showed that its Ca, Mg, and Fe content ranged from 0.39 to 9.22, 2.4 to 6.52, and 1.47 to 7.82 atomic percent respectively (see Table 2), consistent with the formula $Ca(Fe_{0.5}Mg_{0.5})(CO_3)_2$.

4.2.6 Clay minerals

The XRD results indicate that the clay minerals in the CO_2-containing reservoirs of the Yinggehai Basin mainly consist of mixed-layer illite and smectite, and kaolinite (Huang et al., 2004; Jiang et al., 2015;Tong et al., 2012). The mixed layer illite and smectite commonly surround the detrital minerals as "clay rims”, which could be identified by polarizing microscope. Mixed layer illite and smectite are not found in the sandstone pores, suggesting that it is the earliest formed secondary mineral in the diagenetic sequence. Honeycomb-like authigenic clay is seen to grow on K-feldspar (see Fig. 4l, m). According the EDS results shown in Table 3, most of the smectite and mixed layer illite are Ca depleted. This suggests that the Ca in the smectite and mixed

253 layer of illite and smectite may have been removed over time through water-mineral
254 reactions.
255 Authigenic kaolinite grows as vermicular assemblages in the sandstone pores.
256 Hexagonal kaolinite crystals are found attached to dawsonite crystals (Fig. 4n), at times
257 adjacent to small "etch pits" on the dawsonite surface (Fig. 4o), suggesting that some
258 kaolinite post-dates the dawsonite. However, vermicular kaolinite is commonly
259 interspersed between acicular dawsonite crystals, suggesting that this kaolinite formed
260 slightly earlier than or concurrently with dawsonite (Fig. 4p). In some places ankerite
261 grew on the top of kaolinite aggregates (Fig. 4q). This suggests that the formation of
262 kaolinite might have spanned from the period from when dawsonite grew through that
263 of ankerite formation.
264 Chlorite was not observed in the samples considered in this study. Its presence in
265 the rocks of the LDX system was reported by Fu et al. (2016). Moreover, the presence
266 of chlorite within and below the CO_2 gas reservoirs is inferred as a potential source of
267 the iron leading to ankerite precipitation (see below).
268
269 *4.3 Vertical characteristics of authigenic carbonates in the reservoirs*
270 The dawsonite and ankerite contents across the study area, measured on 159 thin
271 sections, are shown in Fig. 5. Over the depths of this study (from 1841.6 m to 1868.89
272 m), dawsonite (0.7 to 8.3%) and ankerite (1.7 to 26.0%) in the LDX-1-1 well mainly
273 developed near the gas water contact (GWC) (Fig. 5a). Owing to lack of samples, few
274 observations of these minerals were made above the GWC in this well. In well
275 LDX-1-4, the limited measurements of mineral content in the gas reservoirs show the
276 dawsonite and ankerite content ranging from 0.7 to 2.3% and 2.0 to 14.0% above the
277 GWC, whereas the corresponding content results for dawsonite and ankerite under the
278 GWC in this well are 1.0 to 6.3% and 1.0 to 24.0 % (Fig. 5b).
279
280 *4.4 C and O isotope compositions*

The stable isotopic compositions of dawsonite and ankerite are shown in Table 4 and Fig. 6. The carbon isotope ($\delta^{13}C$) values for dawsonite vary from -4.3‰ to -0.6‰ with an average value of -2.0‰. The oxygen isotope ($\delta^{18}O$) values for dawsonite range from +22.4‰ to +24.0‰. The $\delta^{13}C$ values for ankerite range from -2.6‰ to -0.8‰ with an average value of -1.4‰ and the $\delta^{18}O$ values range from +22.8‰ to +23.7‰.

The measured $\delta^{13}C$ values of dawsonite and ankerite have been used to estimate the corresponding equilibrium $\delta^{13}C$ of the CO_2 ($\delta^{13}C_{CO2}$) from which they precipitated. The $\delta^{13}C_{CO2}$ for the CO_2 that formed the dawsonite, was estimated assuming dawsonite exhibits an identical CO_2 carbon isotope fractionation as that of calcite, using the equation proposed by Ohmoto and Rye (1972) (Baker et al., 1995). The calculated $\delta^{13}C$ for the CO_2 in equilibrium with ankerite was estimated assuming its fractionation was identical to the dolomite-CO_2 fractionation equation proposed by Horita (2014). The $\delta^{13}C$ of the CO_2 ($\delta^{13}C_{CO2}$) calculated to be in isotopic equilibrium with dawsonite range from -9.66‰ to -6.69‰ with an average value of -7.90‰. The equilibrated $\delta^{13}C_{CO2}$ for ankerite varies from -7.27‰ to -5.94‰ with a mean value of -6.4‰.

The formation temperature for dawsonite and ankerite were calculated from their oxygen isotope compositions. This was done by assuming oxygen fractionation between dawsonite and H_2O is identical to the calcite-H_2O fractionation equation proposed by O'Neil et al. (1969) and that oxygen fractionation between ankerite and H_2O is identical to the dolomite-H_2O fractionation equation of Horita (2014). The ^{18}O value for water used in these calculations was $\delta^{18}O_{H2O}$ = +2.7‰ (Deng and Chen, 1994), which was measured in the formation waters of the DFY-1 structure in the Yinggehai-Huangliu Formation of the Yinggehai basin (Fig. 1). The calculated temperature for dawsonite formation varies from 67.8 ºC to 79.6 ºC and the calculated temperature of ankerite formation ranges from 89.6 ºC to 96.4 ºC (see Table 4). These temperatures are consistent with 1) the earlier formation of dawsonite and 2) the increasing temperature of the study site over time as the basin subsided. Note that the current temperature of the study site is 92 to 103 ^{o}C.

5 Discussion

5.1 The origin of the carbon in the dawsonite and ankerite

The $\delta^{13}C_{CO2}$ of the gas forming dawsonite and ankerite reported above and in Table 4 are similar to the current $\delta^{13}C$ values in the CO_2-rich reservoirs of the LDX system; the current $\delta^{13}C_{CO2}$, are reported to range from -8.2‰ to -4.2‰ (He et al., 2005). Moreover, the hydrogen and oxygen isotopic compositions of the formation water in the Yinggehai Basin reservoirs are significantly different from that of meteoric water, which implies the lack of exchange between meteoric water and that present in the LDX system (Deng and Chen, 1994). Such evidence suggests that the CO_2 in the gas reservoir is likely a major carbon source for the both dawsonite and ankerite formation.

Carbon dioxide in the LDX gas reservoirs at the present time is likely dominated by magmatic derived CO_2. Firstly, the $\delta^{13}C_{CO2}$ value in the gas reservoir ranges from -8.2‰ to -4.2‰, which is significantly different from that obtained from kerogen degradation; $\delta^{13}C_{CO2}$ from kerogen degradation ranges from -25‰ to -20‰ (Irwin et al., 1977; Tissot and Welte, 1984) and CO_2 from bacterial fermentation typically has a $\delta^{13}C_{CO2} \sim +15$‰ (Irwin et al., 1977). Secondly, the carbon isotope values of CO_2 in the LDX system exhibits a $\delta^{13}C_{CO2}$ range similar to the -8‰ to -3‰ range observed for CO_2 sourced from mantle-derived magma (Baker et al., 1995; Clayton et al., 1990; Dai, 1996; Ohmoto and Rye, 1972; Rollinson, 2014;). Taking account of the observations summarized above, we suggest that origin of the CO_2 in the LDX-1 structures is mantle-derived magma degasing.

The timing of dawsonite and ankerite formation can be constrained by the timing of the basaltic magmatism related CO_2 charging of the LDX system. The Yinggehai Formation, where the dawsonite and ankerite developed, was formed between 5.5 Ma and 1.9Ma (Fig. 2). The Honghe fault zone, which controls the formation and distribution direction of Yinggehai basin is still active (Zhu et al., 2009) (Fig. 1). The

ages of alkaline basalt in this region range from 4 to 6 Ma and from 1 Ma up to present (Zhu and Wang, 1989). Several ages of the CO_2 charging into the Yinggehai Formation have been reported in the literature; these ages range from 0.3 to 1.9 Ma (Fu et al., 2016; Huang et al., 2005; Wang et al., 2004; Xie et al., 2014). Based on these ages, it seems reasonable to conclude the dawsonite and ankerite in the Yinggehai Formation is formed during the last 1.9 Ma.

5.2 Cation source of dawsonite and ankerite

The dissolution of feldspars in the LDX-1 structure provides the cations for dawsonite. The formation of dawsonite from feldspar has been observed in numerous systems. For example, feldspars were observed to be altered to dawsonite in the Lam Formation of Shabwa basin Yemen (Worden, 2006), in the reservoirs of the Castillo structure of the Golfo San Jorge basin (Comerio et al., 2014), and in the Songliao basin, the Hailaer basin, and the East Sea basin in China (Gao et al., 2009; Liu et al., 2011; Zhao et al., 2018; Zhou et al., 2014). The reaction forming dawsonite from albite can be written (Bénézeth et al., 2007; Hellevang et al., 2005; Ryzhenko, 2006; Xi et al., 2016):

$$NaAlSi_3O_8 + CO_2 + H_2O \rightleftharpoons NaAlCO_3(OH)_2 + 3SiO_{2(aq)} \quad \text{(Eq. 1)}$$

Albite Dawsonite

where some of the liberated $SiO_{2(aq)}$ could provoke quartz precipitation. The equivalent reaction forming dawsonite from K-feldspar:

$$KAlSi_3O_8 + Na^+ + CO_2 + H_2O \rightleftharpoons NaAlCO_3(OH)_2 + 3SiO_{2(aq)} + K^+ \quad \text{(Eq. 2)}$$

K-feldspar Dawsonite

has been discounted by Hellevang et al. (2011) due to the likely build-up of K^+ in the aqueous phase arresting this reaction.

Evidence for the coupling of feldspar dissolution to dawsonite precipitation reactions could be found throughout the LDX system (Fig. 4c, d, r). If dawsonite originates from K-feldspar by Eq. 2, however, its growth also requires Na^+ from the fluid phase. This would require the system to be relatively open to fluid transport,

365 which may be limited in this system. Note that according to mass conservation, for
366 every 1 cm^3 of dawsonite formed from albite by reaction 1, there should be 1.16 cm^3 of
367 SiO_2 precipitation (Zhou et al., 2014). However, far less microcrystalline quartz is
368 observed in our system than dawsonite (Fig. 4b), which suggests that some of the SiO_2
369 may have been consumed by other water-mineral reactions.

370 Geochemical calculations results suggest that chlorite dissolution provoked by
371 the charging of the system by CO_2 could provide Fe^{2+} for ankerite formation (Xu et al.,
372 2005, 2007, 2014; Yu et al., 2014). The dissolution of smectite also could provide
373 some of the iron for ankerite growth (Hellevang et al., 2013; Pham et al., 2011;
374 Worden and Morad, 2003; Worden, 2006), as well as some aluminum promoting
375 dawsonite formation. The dissolution of chlorite and smectite coupled to ankerite
376 formation has been observed in the sandstone reservoirs of the Otway basin of
377 Austrailia,, in the Songliao Basin of China, the Jurassic and late Cretaceous reservoirs
378 of North Sea oil fields, and in the Eocene strata from Wilcox of Texas, (Awwiller,
379 1993; Hendry et al., 2000; Liu et al., 2011; Thyberg et al., 2010; Watson et al., 2004).
380 The chlorite content of the Yinggehai Basin CO_2 bearing reservoirs has been reported
381 to be significantly lower than that in CO_2–free reservoirs (Tong et al., 2012). Similar
382 observations have been reported in wells of the Yinggehei Basin (Huang et al., 2004;
383 Jiang et al., 2015). Such observations suggest that the dissolution of iron bearing clay
384 minerals such as chlorite is the main Fe^{2+} source for ankerite. The Mg^{2+} and some
385 Ca^{2+} in the ankerite crystals could come from dolomite dissolution, as fresh ankerite is
386 observed growing within a dolomite matrix (Fig. 4i). Additional Ca^{2+} can be sourced
387 from the transformation of clays in the system; a number of studies have reported Ca
388 release as smectite transforms to mixed layered clays and illite (e.g. Boles and Frank,
389 1979; McHargue and Price, 1982). A close relation between ankerite and smectite is
390 evident in the studied core samples (see Fig. 7). Taking account of these observations,
391 a representative reaction coupling chlorite dissolution to ankerite precipitation could
392 be expressed as (modified from Kirste et al., 2004; see also Luquot et al., 2012):

393 $Fe_2Al_2SiO_5(OH)_4$ + 2 $Ca(MgCO_3)_2$ + SiO_2 + 2 Ca^{2+} + 4 CO_2 +2 H_2O =

394 Chamosite Dolomite Quartz

395 4 $Ca(Fe_{0.5}Mg_{0.5})(CO_3)_2$ + $Al_2Si_2O_5(OH)_4$ + 4 H^+ (Eq. 3) Ankerite

396 Kaolinite

397 Note this reaction, balanced on Fe and Mg, requires substantial magmatic CO_2 for
398 ankerite formation, consistent with its carbon isotope composition. This reaction also
399 consumes SiO_2, which may account, at least in part, for the low mass of authigeic
400 quartz in the present day system.

401

402 *5.3 CO_2 partial pressure and carbonate mineral stability*

403 It is likely that both ankerite and dawsonite are formed after the arrival of mantle
404 sourced CO_2, providing a clear analogy for modern carbon capture and storage
405 systems. The observations described in this study indicate that dawsonite is first
406 formed at ~70 ºC, followed by ankerite at ~ 90 °C, in response to the arrival of CO_2
407 into the overlying reservoirs. The increase in temperature in the system likely stems
408 from its increased burial depth over time. Ankerite is also reported to be the last
409 forming mineral in the sandstone reservoirs in Songliao (Liu et al., 2011; Yu et al.,
410 2015) and Hailaer basins (Gao et al., 2009). Some kaolinite is seen to precipitate
411 coupled to the dissolution of dawsonite; some dissolution etch pits on dawsonite
412 crystal were evident near the kaolinite (Fig. 4m). Kaolinite precipitation continues as
413 ankerite precipitates, consistent with Eq. (3). The formation of ankerite also appears
414 to be linked to dolomite dissolution.

415 All of these observations are consistent with the phase diagrams shown in Figs. 8
416 to 10. In Fig. 8, the relative stability of dawsonite in the Na_2O-Al_2O_3-SiO_2-CO_2-H_2O
417 system balanced on aluminum and saturated with quartz is shown. Dawsonite and
418 quartz become stable relative to albite at log (f_{CO2}) > 0.15 and 0.9 at 70 and 100 °C,
419 respectively. This diagram thus suggests that albite would be favored to transform to
420 dawsonite as CO_2 fills the reservoirs in accord with reaction 1. As suggested by Fig. 9,

some of the precipitated dawsonite and quartz will tend to react to form kaolinite due to an increase in temperature, which tends to shrink the dawsonite stability field. The value of log (f_{CO2}) in equilibrium with the assemblage albite = dawsonite + quartz at 70 and 100 °C plot as vertical lines on the Fig. 10, which also shows the relative stability field of ankerite + kaolinite relative to that of chlorite, dolomite and quartz consistent with reaction 3. It can be seen that for all a_{Ca2+}/a^2_{H+} > ~9.7 at 70 °C and > ~7.3 at 100 °C, dawsonite would first tend to form before ankerite as the CO_2 partial pressure in the reservoirs increase. The partial pressure of CO_2 in the LDX system would increase as the CO_2 fraction of the gas progressively increased in the reservoirs located just above the studied rock samples (Fig. 5). The persistence of dawsonite and ankerite in this system is assured by the continued presence of the CO_2-rich gas reservoir, which maintains f_{CO2} at relatively high levels. Note the current temperature of the gas reservoirs are 92.3 and 102.9 ºC for well LDX-1-4 and well LDX-1-1 respectively, and the corresponding gas pressure in reservoirs, which is dominated by CO_2, are between 18.9 and 43.2 Mpa (China National Offshore Oil Company, personal communication). Hellevang et al. (2005), noted, that dawsonite, would likely rapidly dissolve once it became thermodynamically unstable as the f_{CO2} decreased in the such systems.

5.4 The paragenetic sequence

Based on the observations described above, the proposed paragenetic sequence for the studied dawsonite-bearing sandstones is shown in Fig. 11. Secondary clays (mainly illite and smectite mixed layer clays) began forming before compaction during the early stage of diagenesis and coated detrital minerals as clay rims. Sideite is found to form next; siderite precipitation is readily observed in reducing, non-sulphidic pore waters in the suboxic and methanogenesis zones (Morad, 1998). Quartz overgrowths are then observed to form, perhaps due to the recrystallization of biogenic SiO_2, but also accompanied with the formation of minor kaolinite in response to feldspar dissolution.

Subsequently, dolomite is observed to form, potentially promoted by Ca and Mg release from the dissolution or transformation of the earlier formed clays. After the influx of CO_2 into the reservoir. dawsonite and additional quartz forms from the dissolution of feldspar, and subsequently ankerite and kaolinite forms from the dissolution of dolomite, quartz, chlorite and potentially some clay minerals..

5.5 Implications for carbon storage in sandstone reservoirs

The formation and long-term stability of dawsonite and ankerite in the LDX system are likely good analogies for some modern carbon storage systems such as the Shenhua CCS demonstration project in China (Yang et al., 2017). The distribution of dawsonite and ankerite in the LDX reservoirs (Fig. 5) indicates that these minerals can form in the water layers beneath gas water contact (GWC). Some dawsonite and ankerite were also observed above the present day GWC, which may indicate that either 1) the position of the GWC has changed over time or 2) that these phases grew in the gas filled section of the reservoir, potentially on water-wet surfaces. This later, process, however, is likely limited as the dawsonite and ankerite forming reactions 1 and 3 consume H_2O. The formation of such carbonate minerals adjacent to the CO_2 gas reservoir is also supported by the results of TOUGHREACT calculations reported by Pan et al. (2017) that suggest that when CO_2 is injected into sandstone reservoirs, carbonate minerals would form on both upper and lower layers of the reservoir. Carbonate mineral precipitation in the water layers below the GWC has also been observed in New Zealand sandstone reserviors (Higgs et al., 2015). As such, we suggest that the CO_2 in the gas reservior maintains a sufficient CO_2 partial pressure in the formation waters below the GWC to promote the growth and long term stability of dawsonite and ankerite. However, according to the paragenetic sequence determined in this study, kaolinite precipitated from the fluid concurrently with the precipitation of dawsonite and ankerite. Numerous petrographic observations and experimental simulations suggest that kaolinite and dawsonite formation could significantly reduce

sandstone permeability (Luquot et al., 2012; Shiraki and Dunn, 2000; Yu et al., 2012). Kaolinite also commonly grows in response to CO_2-feldspar or CO_2-clay mineral interaction (Luquot et al., 2012; Moore et al., 2005; Shiraki and Dunn, 2000; Yu et al., 2012). Shiraki and Dunn (2000) concluded that the precipitation and growth of kaolinite in the pores could block pore throats leading to the reduction of the permeability of reservoir. Similarly, Worden (2006) suggested that the fiber-like crystal morphology of dawsonite would also reduce sandstone permeability. The reduced permeability in the sandstone could slow chemical transport, and including potentially the transport of dissolved CO_2 out of the storage system. Such processes could thereby promote the stability of carbonate minerals in this system. The decrease in permeability could also lead to fluid pressure build up in the gas reservoir as further minerals form in this system.

6 Conclusions

This study focused on the mineral reactions provoked by the influx of CO_2 into the subarkose and sublitharenite sandstones of the Yinggehai basin. This system is likely a good analogy for subsurface carbon storage in sandstone hosted hydrocarbon reservoirs as the influxed CO_2 replaces a methane-rich gas phase in an anticlinal structure. This leads to the presence of a CO_2-rich gas phase stable over a ~1-2 million year time frame. The influx of provoked the CO_2 provoked the formation of dawsonite from plagioclase and ankerite and kaolinite likely from chlorite, quartz, and dolomite, at temperatures of 68 to 80 ºC. and 90 to 96^{o} C, respectively, largely just below the CO_2-gas water interface. The formation of such phases could provide for the mineral storage of some of the CO_2 injected during subsurface carbon storage efforts.

The key to maintaining dawsonite and ankerite stability in such systems appears to be preserving a high partial pressure of CO_2. As such, although the formation of these minerals might lead to the storage of CO_2 injected into sandstones as part of engineered geologic storage efforts, such minerals may not provide for the 'permanent'

mineral storage of this gas that one might anticipate from the formation of carbonate minerals such as calcite, which can be stable at far lower CO_2 partial pressure, unless the system tends to become impermeable as due to the formation of various secondary minerals.

Acknowledgement

This manuscript is sponsored by the National Natural Science Foundation of China (No. 41572082), the China Scholarship Council and the project "Study on CO_2 accumulation in reservoirs and the risk assessment for key exploration regions of Chinese sea areas (No. YXKY-2015-ZY-01)" from China National Offshore Oil Corporation (CNOOC).

References

Awwiller, D., 1993. Illite/smectite formation and potassium mass transfer during burial diagenesis of mudrocks: A study from the Texas Gulf Coast Paleocene-Eocene. Journal of Sedimentary Research 63(3): 501-512.

Bachu, S., 2003. Screening and ranking of sedimentary basins for sequestration of CO_2 in geological media in response to climate change. Environmental Geology, 44(3): 277-289.

Bachu, S., Gunter, W., Perkins, E., 1994. Aquifer disposal of CO_2: hydrodynamic and mineral trapping. Energy Conversion and Management 35(4): 269-279.

Baker, J.C., Bai, G.P., Hamilton, P.J., Golding, S.D., Keene, J.B., 1995. Continental-scale magmatic carbon dioxide seepage recorded by dawsonite in the Bowen-Gunnedah-Sydney Basin system, eastern Australia. Journal of Sedimentary Research 65(3): 522-530.

Barnes, C.S., 2006. ThermoSolver: an integrated educational thermodynamics software program. H.B. Thesis Abstr., 46p.

Becker, R.H., 1971. Carbon and Oxygen Isotope Ratios in Iron-formation and Associated Rock from the Hammersley Range of Western Australia and Their Implications, Ph.D.Thesis University of Chicago.

Bénézeth, P., Palmer, D.A., Anovitz, L.M., Horita, J., 2007. Dawsonite synthesis and reevaluation of its thermodynamic properties from solubility measurements: Implications for mineral trapping of CO_2. Geochimica et Cosmochimica Acta 71(18): 4438-4455.

539 Benson, S.M., Cole, D.R., 2008. CO_2 Sequestration in Deep Sedimentary Formations.
540 Elements 4(5): 325-331.

541 Boles, J.R., Franks, S.G., 1979. Clay diagenesis in Wilcox Sandstones of Southwest
542 Texas: Implications of smectite disgenesis on sandstone cementation. J. Sed. Pet.
543 49(1): 55-70.

544 Clayton, J., Spencer, C., Koncz, I., Szalay, A., 1990. Origin and migration of
545 hydrocarbon gases and carbon dioxide, Bekes Basin, southeastern Hungary.
546 Organic Geochemistry 15(3): 233-247.

547 Comerio, M., Morosi, M.E., Tunik, M., Paredes, J.M., Zalba, P.E., 2014. The Role of
548 Telogenetic Injection of Magmatically Derived CO_2 in the Formation of
549 Dawsonite from the Castillo Formation, Chubut Group, Patagonia, Argentina. The
550 Canadian Mineralogist 52(3): 513-531.

551 Dai, J., 1996. CO_2 reservoir and its type in eastern China and continental shelf. Nature
552 Explore,15(4): 18-20 (in Chinese).

553 Deng, X., Chen, M., 1994. A research on the formation water chemical characteristics
554 in Yinggrhai basin of South China sea and its significance in petroleum geology.
555 Scientia Geologica Sinica 29(4): 404-407 (in Chinese with English abstr.).

556 Dickson, J., 1965. A modified staining technique for carbonates in thin section. Nature
557 205(4971): 587-587.

558 Fischer, S., Liebscher, A., Wandrey, M., 2010. CO_2-brine-rock interaction — First
559 results of long-term exposure experiments at in situ P-T conditions of the Ketzin
560 CO_2 reservoir. Chemie der Erde 70: 155-164.

561 Folk, R.L., 1968. Petrology of Sedimentary rocks. Hemphill's. Austin, Texas, 182 pp.

562 Fu, M., Song, R., Xie, Y., Zhang, S., Gluyas, J., Zhang, Y., Zhang, Y., 2016. Diagenesis
563 and reservoir quality of overpressured deep-water sandstone following inorganic
564 carbon dioxide accumulation: Upper Miocene Huangliu Formation, Yinggehai
565 Basin, South China Sea. Marine and Petroleum Geology 77: 954-972.

566 Gao, Y., Liu, L., Hu, W., 2009. Petrology and isotopic geochemistry of
567 dawsonite-bearing sandstones in Hailaer basin, northeastern China. Applied
568 Geochemistry 24(9): 1724-1738.

569 Gaus, I., Le Guern, C., Pearce, J., Pauwels, H., Shepherd, T., Hatziynnis, G., Metaxas,
570 A., 2005. Comparison of long-term geochemical interactions at two natural
571 CO_2-analogues: Montmiral (Southeast Basin, France) and Messokampos (Florina
572 Basin, Greece) case studies, Greenhouse Gas Control Technologies 7. Elsevier, pp.
573 561-569.

574 Golab, A.N., Carr, P.F., Palamara, D.R., 2006. Influence of localised igneous activity on
575 cleat dawsonite formation in Late Permian coal measures, Upper Hunter Valley,
576 Australia. International Journal of Coal Geology 66(4): 296-304.

577 Gong, Z., Yang, J., Yang, Z., 1997. The major oil and gas fields of China offshore.
578 Petroleum Industry Press, Beijing (in Chinese).

579 Hao, F., Li, S., Dong, W., Hu, Z., Huang, B., 1998. Abnormal organic- matter
580 maturation in the Yinggehai Basin, South China Sea: Implications for
581 hydrocarbon expulsion and fluid migration from overpressured systems. Journal
582 of Petroleum Geology,21(4): 427-444.

583 He, J., Xia, B., Liu, B., Zhang, S., 2005. Origin, migration and accumulation of CO_2 in
584 East China and offshore shelf basins. Petroleum Exploration and Development
585 32(4): 663-673 (in Chinese with English abstr.).

586 Hellevang, H., Aagaard, P., Oelkers, E.H., Kvamme, B., 2005. Can dawsonite
587 permanently trap CO_2? Environmental Science & Technology 39(21): 8281-8287.

588 Hellevang, H., Declercq, J., Aagaard, P., 2011. Why is Dawsonite Absent in CO_2
589 Charged Reservoirs? Oil Gas Sci. Technol. – Rev. IFP Energies Nouvelles 66(1):
590 119-135.

591 Hellevang, H., Pham, V.T.H., Aagaard, P., 2013. Kinetic modelling of CO_2-water-rock
592 interactions. International Journal of Greenhouse Gas Control 15: 3-15.

593 Hendry, J.P., Wilkinson, M., Fallick, A.E., Haszeldine, R.S., 2000. Ankerite
594 cementation in deeply buried Jurassic sandstone reservoirs of the central North
595 Sea. Journal of Sedimentary Research 70(1): 227-239.

596 Higgs, K.E., Funnell, R.H., Reyes, A.G., 2013. Changes in reservoir heterogeneity and
597 quality as a response to high partial pressures of CO_2 in a gas reservoir, New
598 Zealand. Marine and Petroleum Geology 48: 293-322.

599 Higgs, K.E., Haese, R.R., Golding, S.D., Schacht, U., Watson, M.N., 2015. The Pretty
600 Hill Formation as a natural analogue for CO_2 storage: An investigation of
601 mineralogical and isotopic changes associated with sandstones exposed to low,
602 intermediate and high CO_2 concentrations over geological time. Chemical
603 Geology 399: 36-64.

604 Hitchon, B. (Ed.), 1996. Aquifer disposal of carbon dioxide: hydrodynamic and mineral
605 trapping-proof of concept, Geoscience Publishing, Ltd, Sherwood Park,
606 Alberta,Canada, 165 pp

607 Hoang, N., Flower, M.F., 1998. Petrogenesis of Cenozoic basalts from Vietnam:
608 implication for origins of a ‘diffuse igneous province’. Journal of Petrology 39(3):
609 369-395.

610 Hoang, N., Flower, M.F., Carlson, R.W., 1996. Major, trace element, and isotopic
611 compositions of Vietnamese basalts: Interaction of hydrous EM1-rich
612 asthenosphere with thinned Eurasian lithosphere. Geochimica et Cosmochimica
613 Acta 60(22): 4329-4351.

614 Horita, J., 2014. Oxygen and carbon isotope fractionation in the system

615 dolomite-water-CO_2 to elevated temperatures. Geochimica et Cosmochimica Acta
616 129: 111-124.

617 Huang, B., Li, X., Yi, P., Xiao, X., 2005. Geochemical behaviors and reservoiring
618 history of natural gas in Ledong gas field in Yinggehai basin. Oil and Gas Geology
619 26(4): 524-529 (in Chinese with English abstr.).

620 Huang, B., Xiao, X., Li, X., 2003. Geochemistry and origins of natural gases in the
621 Yinggehai and Qiongdongnan basins, offshore South China Sea. Organic
622 Geochemistry 34(7): 1009-1025.

623 Huang, B., Xiao, X., Li, X., Cai, D., 2009. Spatial distribution and geochemistry of the
624 nearshore gas seepages and their implications to natural gas migration in the
625 Yinggehai Basin, offshore South China Sea. Marine and Petroleum Geology 26(6):
626 928-935.

627 Huang, B., Xiao, X., Zhu, W., 2004. Geochemistry, origin, and accumulation of CO_2 in
628 natural gases of the Yinggehai Basin, offshore South China Sea. AAPG Bulletin
629 88(9): 1277-1293.

630 IPCC, 2005. Underground geological storage, in Carbon dioxide capture and storage,
631 Metz B., Davidson O., de Coninck H., Loos M., Meyer L. (eds), Cambridge
632 University Press, Cambridge, UK, pp. 431.

633 IPCC, 2007. Impacts, adaption and vulnerability, Parry M.L., Canziani O.F., Palutikof
634 J.P., van der Linden P.J., Hanson C.E. (eds), Cambridge University Press,
635 Cambridge, UK, pp. 976.

636 Irwin, H., Curtis, C., Coleman, M., 1977. Isotopic evidence for source of diagenetic
637 carbonates formed during burial of organic-rich sediments. Nature 269: 209.

638 Jiang, T., Xie, X., Chen, H., Wang, Z., Li, X., 2015. Geochemistry of pore water and
639 associated diagenetic reactions in the diapiric area of Yinggehai basin,
640 northwestern South China Sea. Journal of Earth Science, 26(3): 306-316.

641 Johnson, J.W., Nitao, J.J., Steefel, C.I., Knauss, K.G., 2001. Reactive Transport
642 Modeling of Geologic CO_2 Sequestration in Saline Aquifers: The Influence of
643 Intra-Aquifer Shales and the Relative Effectiveness of Structural, Solubility, and
644 Mineral Trapping During Prograde and Retrograde Sequestration, First National
645 Conference on Carbon Sequestration. National Energy Technology Laboratory,
646 Washington, DC.

647 Klajmon, M., Havlová, V., Červinka, R., Mendoza, A., Franců, J., Berenblyum, R.,
648 Arild, Ø., 2017. REPP-CO_2: Equilibrium Modelling of CO_2-Rock-Brine Systems.
649 Energy Procedia 114: 3364-3373.

650 Kirste, D.M., Watson, P.R., Tingate, P.R., 2004. Geochemical modelling of
651 CO_2-water-rock interaction in the Pretty Hill fomation, Otway Basin. In Boult,
652 P.J., Johns, D.R., Lng, S.C. (eds.), Eastern Austrailia basins symposium II.

653 Special publication 19-22, Petroleum Exploration Society of Austrailia, Adelaine,
654 Sputh Austrailia, pp. 404-411.

655 Lackner, K.S., Wendt, C.H., Butt, D.P., Joyce, E.L., Sharp, D.H., 1995. Carbon
656 dioxide disposal in carbonate minerals. Energy 20(11): 1153-1170.

657 Li, C., Wang, F., Zhong, C., 2005. Geochemistry of Quaternary basaltic volcanic rocks
658 of Weizhou island in Beihai City of Guangxi and a discussion on characteristics of
659 their source. Acta Petrologica et Mineralogica 24(1): 1-11 (in Chinese with
660 English abstr.).

661 Liu, N. Liu, L., Qu, X., Yang, H., Wang, L., Zhao, S., 2011. Genesis of authigene
662 carbonate minerals in the Upper Cretaceous reservoir, Honggang Anticline,
663 Songliao Basin: A natural analog for mineral trapping of natural CO_2 storage.
664 Sedimentary Geology 237(3-4): 166-178.

665 Luo, X., Dong, W., Yang, J., Yang, W., 2003. Overpressuring mechanisms in the
666 Yinggehai basin, south China sea. AAPG bulletin, 87(4): 629-645.

667 Luquot, L., Andreani, M., Gouze, P., Camps, P., 2012. CO_2 percolation experiment
668 through chlorite/zeolite-rich sandstone (Pretty Hill Formation-Otway
669 Basin-Australia). Chemical Geology 294-295: 75-88.

670 McCrea, J.M., 1950. On the isotopic chemistry of carbonates and a paleotemperature
671 scale. The Journal of Chemical Physics 18(6): 849-857.

672 McHargue, T.R., Price, R.C., 1982. Dolomie from clay in argillaceous or
673 shale-assocaited maring carbonates. J. Sed. Pet. 52(3): 873-886.

674 Manabe, S., Stouffer, R.J., 1993. Century-scale effects of increased atmospheric CO_2
675 on the ocean-atmosphere system. Nature, 364(6434): 215-218.

676 Matter, J.M., Stute, M., Snæbjörnsdottir, S.Ó., Oelkers, E.H., Gislason, S.R., Aradottir,
677 E.S., Sigfusson, B., Gunnarsson, I., Sigurdardottir, H., Gunnlaugsson, E.,
678 Axelsson, G., Alfredsson, H.A., Wolff-Boenisch, D., Mesfin, K., Fernandez de la
679 Reguera Tayà, D., Hall, J., Dideriksen, K. and Broecker, W.S. (2016) Rapid
680 carbon mineralization for permanent disposal of anthropogenic carbon dioxide
681 emissions. Science 352: 1312-1314

682 Meng, F., Xiao, L., Xie, Y., Wang, Z., Liu, J., Tong, C., Zhang, H., Gao, Y., Meng, Y.,
683 Wei, W., 2012. Abnormal Transformation of the Clay Minerals in Yinggehai Basin
684 and Its Significances. Acta Sedimentologica Sinica 30(3): 469-476 (in Chinese
685 with English abstr.).

686 Ming, X., Liu, L., Yu, L., Bai, H., Yu, Z., Liu, N., Yang, H., Wang, F., Li, B., 2017.
687 Thin-film dawsonite in Jurassic coal measure strata of the Yaojie coalfield, Minhe
688 Basin, China: A natural analogue for mineral carbon storage in wet supercritical
689 CO_2. International Journal of Coal Geology 180: 83-99.

690 Moore, J., Adams, M., Allis, R., Lutz, S., Rauzi, S., 2005. Mineralogical and

691 geochemical consequences of the long-term presence of CO_2 in natural reservoirs:
692 An example from the Springerville-St. Johns Field, Arizona, and New Mexico,
693 U.S.A. Chemical Geology 217(3-4): 365-385.

694 Morad, S., 1998. Carbonate cementation in sandstones: distribution patterns and
695 geochemical evolution. In: Morad, S. (Ed.), Carbonate Cement in Sandstone
696 Reservoirs. Special Publication of the International Association of
697 Sedimentologists, 26, pp. 1–26.

698 O'Neil, J.R., Clayton, R.N., Mayeda, T.K., 1969. Oxygen isotope fractionation in
699 divalent metal carbonates. The Journal of Chemical Physics 51(12): 5547-5558.

700 Oelkers, E.H., Cole, D.R., 2008. Carbon dioxide sequestration a solution to a global
701 problem. Elements 4(5): 305-310.

702 Oelkers, E.H., Gislason, S.R., Matter, J., 2008. Mineral Carbonation of CO_2. Elements
703 4(5): 333-337.

704 Ohmoto, H., Rye, R., 1972. Isotopes of sulfur and carbon. In *Geochemistry of*
705 *Hydrothermal Ore Deposits* (ed. H. L. Barnes), pp. 509-567. John Wiley, New
706 York.

707 Pan, F., McPherson, B.J., Kaszuba, J., 2017. Evaluation of CO_2-Fluid-Rock Interaction
708 in Enhanced Geothermal Systems: Field-Scale Geochemical Simulations.
709 Geofluids 2017: 1-11.

710 Parkhurst, D.L., Appelo, C., 2013. Description of input and examples for PHREEQC
711 version 3--A computer program for speciation, batch-reaction, one-dimensional
712 transport, and inverse geochemical calculations. U.S. Geol. Surv. Techiques
713 Methods 6-A43, 497 p. <http://pubs.usgs.gov/tm/06/a43>.

714 Pauwels, H., Gaus, I., Le Nindre, Y.M., Pearce, J., Czernichowski-Lauriol, I., 2007.
715 Chemistry of fluids from a natural analogue for a geological CO_2 storage site
716 (Montmiral, France): lessons for CO_2-water-rock interaction assessment and
717 monitoring. Applied Geochemistry 22(12): 2817-2833.

718 Pearce, J.K., Dawson, G.K.W., Law, A.C.K., Biddle, D., Golding, S.D., 2016.
719 Reactivity of micas and cap-rock in wet supercritical CO_2 with SO_2 and O_2 at CO_2
720 storage conditions. Applied Geochemistry 72: 59-76.

721 Pham, V.T.H., Lu, P., Aagaard, P., Zhu, C., Hellevang, H., 2011. On the potential of
722 CO_2-water-rock interactions for CO_2 storage using a modified kinetic model.
723 International Journal of Greenhouse Gas Control 5(4): 1002-1015.

724 Power, I.M., Harrison, A.L., Dipple, G.M., Wilson, S.A., Kelemen, P.B., Hitch, M.,
725 Southam, G., 2013. Carbon mineralization: from natural analogues to engineered
726 systems. Reviews in Mineralogy and Geochemistry 77(1): 305-360.

727 Rollinson, H., 2014. Using geochemical data: evaluation, presentation, interpretation.
728 Routledge, Interpretation. Longman, London. 352 pp.

729 Rosenbaum, J., Sheppard, S., 1986. An isotopic study of siderites, dolomites and
730 ankerites at high temperatures. Geochimica et Cosmochimica Acta, 50(6):
731 1147-1150.

732 Ryzhenko, B., 2006. Genesis of dawsonite mineralization: Thermodynamic analysis
733 and alternatives. Geochemistry International 44(8): 835-840.

734 Sharma, T., Clayton, R.N., 1965. Measurement of O^{18}/O^{16} ratios of total oxygen of
735 carbonates. Geochimica et Cosmochimica Acta 29(12): 1347-1353.

736 Shiraki, R., Dunn, T.L., 2000. Experimental study on water-rock interactions during
737 CO_2 flooding in the Tensleep Formation, Wyoming, USA. Applied Geochemistry
738 15(3): 265-279.

739 Sun, Y., Wang, Y., 2000. Main gas sources and gas charge history in
740 Yinggehai-Qiongdongnan region. China Offshore Oil And Gas (Geology) 14(4):
741 240-247 (in Chinese with English abstr.).

742 Thyberg, B., Jahren, J., Winje, T., Bjørlykke, K., Faleide, J.I., Marcussen, Ø., 2010.
743 Quartz cementation in Late Cretaceous mudstones, northern North Sea: Changes
744 in rock properties due to dissolution of smectite and precipitation of micro-quartz
745 crystals. Marine and Petroleum Geology 27(8): 1752-1764.

746 Tissot, B.P., Welte, D.H., 1984. From kerogen to petroleum, Petroleum formation and
747 occurrence. Springer, pp. 160-198.

748 Tong, C., Wang, Z., Li, X., 2012. Pooling conditions of gas reservoirs in the Dongfang
749 1-1 Gas Field,Yinggehai Basin. Natural Gas Industry 32(8): 11-15 (in Chinese
750 with English abstr.).

751 Uysal, I.T., Golding, S.D., Bolhar, R., Zhao, J., Feng, Y., Baublys, K.A., Greig, A.,
752 2011. CO_2 degassing and trapping during hydrothermal cycles related to
753 Gondwana rifting in eastern Australia. Geochimica et Cosmochimica Acta 75(19):
754 5444-5466.

755 Van Pham, T.H., Aagaard, P., Hellevang, H., 2012. On the potential for CO_2 mineral
756 storage in continental flood basalts-PHREEQC batch-and 1D diffusion-reaction
757 simulations. Geochemical Transactions 13(1): 5.

758 Wan, Z., Xia, B., He, J., Liu, B., 2007. The comparative study of hydrocarbon
759 accumulation conditions in Yinggehai and Qiongdongnan basins, Northern South
760 China Sea. Natural Gas Geoscience 18(5): 648-652 (in Chinese with English
761 abstr.).

762 Wang, J., Yin, A., Harrison, T.M., Grove, M., Zhang, Y., Xie, G., 2001. A tectonic
763 model for Cenozoic igneous activities in the eastern Indo-Asian collision zone.
764 Earth and Planetary Science Letters 188(1): 123-133.

765 Wang, Z., He, J., Xie, X., 2004. Heat flow action and its control on natural gas
766 migration and accumulation in mud-fluid diapir areas in Yinggehai basin. Earth

Science 29(2): 203-210 (in Chinese with English abstr.).

Wang, Z., Huang, B., 2008. Dongfang 1-1 gas field in the mud diapir belt of the Yinggehai Basin, South China Sea. Marine and Petroleum Geology 25(4): 445-455.

Watson, M.N., Zwingmann, N., Lemon, N.M., 2004. The Ladbroke Grove-Katnook carbon dioxide natural laboratory: A recent CO_2 accumulation in a lithic sandstone reservoir. Energy 29(9-10): 1457-1466.

Worden, R., Morad, S., 2003. Clay minerals in sandstones: A review of the detrital and diagenetic sources and evolution during burial. Clay Mineral Cement in Sandstones 34: 3-41.

Worden, R.H., 2006. Dawsonite cement in the Triassic Lam Formation, Shabwa Basin, Yemen: A natural analogue for a potential mineral product of subsurface CO_2 storage for greenhouse gas reduction. Marine and Petroleum Geology 23(1): 61-77.

Xi, K., Cao, Y., Zhu, R., Haile, B.G., Hellevang, H., 2016. Evidences of localized CO_2-induced diagenesis in the Cretaceous Quantou Formation, southern Songliao Basin, China. International Journal of Greenhouse Gas Control 52: 155-174.

Xie, Y., Zhang, Y., Xu, D., Gan, J., 2014. Natural gas origin and accumulation model in major and excellent gas fields with high temperature and overpressure in Yinggehai basin:a case of DF13-2 gas field. China Offshore Oil and Gas 26(2): 1-5 (in Chinese with English abstr.).

Xu, T., Apps, J.A., Pruess, K., 2004. Numerical simulation of CO_2 disposal by mineral trapping in deep aquifers. Applied Geochemistry 19(6): 917-936.

Xu, T., Apps, J.A., Pruess, K., 2005. Mineral sequestration of carbon dioxide in a sandstone-shale system. Chemical Geology 217(3-4): 295-318.

Xu, T., Apps, J.A., Pruess, K., Yamamoto, H., 2007. Numerical modeling of injection and mineral trapping of CO_2 with H_2S and SO_2 in a sandstone formation. Chemical Geology 242(3-4): 319-346.

Xu, T., Feng, G., Shi, Y., 2014. On fluid–rock chemical interaction in CO_2-based geothermal systems. Journal of Geochemical Exploration 144: 179-193.

Xu, T., Kharaka, Y.K., Doughty, C., Freifeld, B.M., Daley, T.M., 2010. Reactive transport modeling to study changes in water chemistry induced by CO_2 injection at the Frio-I Brine Pilot. Chemical Geology 271(3-4): 153-164.

Yu, M., Liu, L., Yu, Z., Liu, N., Yang, H., Qu, X., 2014. Dawsonite fixation of mantle CO_2 in the cretaceous Songliao Basin, Northeast China: a natural analogue for CO_2 mineral trapping in oilfields. International Geology Review 56(14): 1792-1812.

Yang, G., Li, Y., Atrens, A., Liu, D., Wang, Y., Jia, L., Lu, Y., 2017. Reactive transport

modeling of long-term CO_2 sequestration mechanisms at the Shenhua CCS demonstration project, China Journal of Earth Science, 28(3): 457-472.

Yu, Z., Liu, L., Liu, K., Yang, S., Yang, Y., 2015. Petrological characterization and reactive transport simulation of a high-water-cut oil reservoir in the Southern Songliao Basin, Eastern China for CO_2 sequestration. International Journal of Greenhouse Gas Control 37: 191-212.

Yu, Z., Liu, L., Yang, S., Li, S., Yang, Y., 2012. An experimental study of CO_2-brine-rock interaction at in situ pressure-temperature reservoir conditions. Chemical Geology 326-327: 88-101.

Zhao, S., Liu, L., Liu, N., 2018. Petrographic and stable isotopic evidences of CO_2 -induced alterations in sandstones in the Lishui sag, East China Sea Basin, China. Applied Geochemistry 90: 115-128.

Zhou, B. Liu, L., Zhao, S., Ming, X., Oelkers, E.H., Yu, Z., Zhu, D., 2014. Dawsonite formation in the Beier Sag, Hailaer Basin, NE China tuff: A natural analog for mineral carbon storage. Applied Geochemistry 48: 155-167.

Zhu, B., Wang, H., 1989. Nd-Sr-Pb isotopic and chemical evidence for the volcanism with MORB-OIB source characteristics in the Leiqiong area. Geochimica 3: 193-201 (in Chinese with English abstr.).

Zhu, M., Graham, S., McHargue, T., 2009. The Red River Fault zone in the Yinggehai Basin, South China Sea. Tectonophysics 476(3-4): 397-417.

Zhu, W., Wu, G., Li, M., 2004. Palaeolimology and hydrocarbon potential in Beibu gulf basin of South China Sea. Oceanologia et Limnologia Sinica 35(1): 8-14 (in Chinese with English abstr.).

Zhu, W., Zhang, G., Yang, S., 2007. North continental margin basin in the south China sea. Petroleum Industry Press Beijing (in Chinese).

Zimmer, K., Zhang, Y., Lu, P., Chen, Y., Zhang, G., Dalkilic, M., Zhu, C., 2016. SUPCRTBL: A revised and extended thermodynamic dataset and software package of SUPCRT92. Computers & Geosciences 90: 97-111.

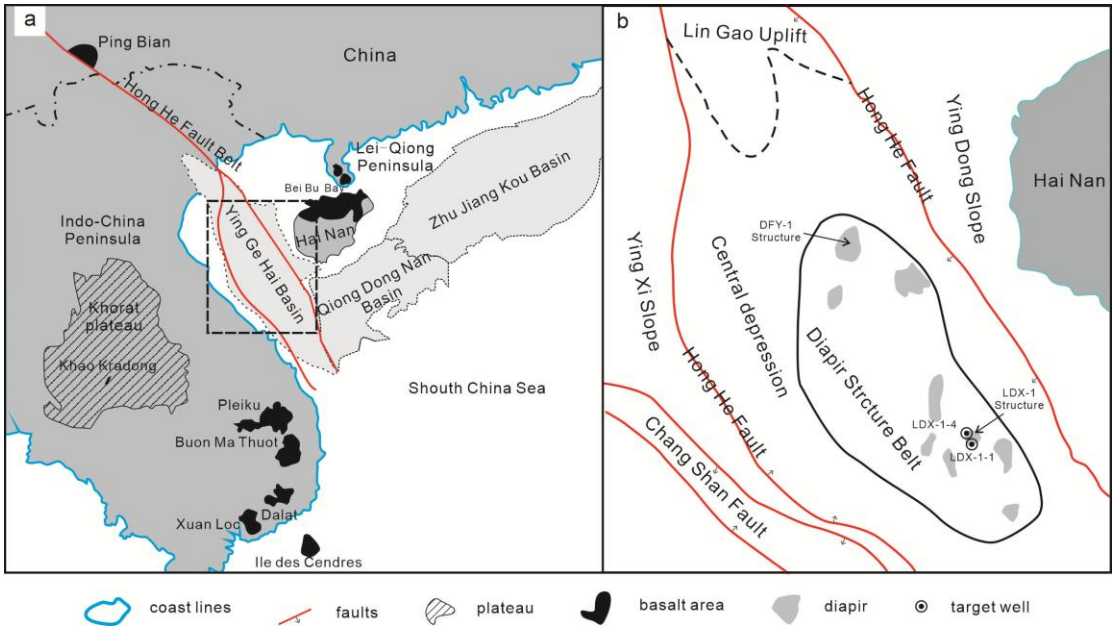

Figure 1. Location map of LDX-1 structure in Yinggehai Basin, south China Sea area. a) The location of Yinggehai basin and basalt area modified after Shi and Yan (2011), basalt areas are modified from Hoang et al. (1996, 1998), Li et al. (2005), Wang et al. (2001); Zhou et al. (1997) and Zhu et al. (1989), b) Geotectonic units modified after Luo et al., (2003) and Meng et al. (2012).

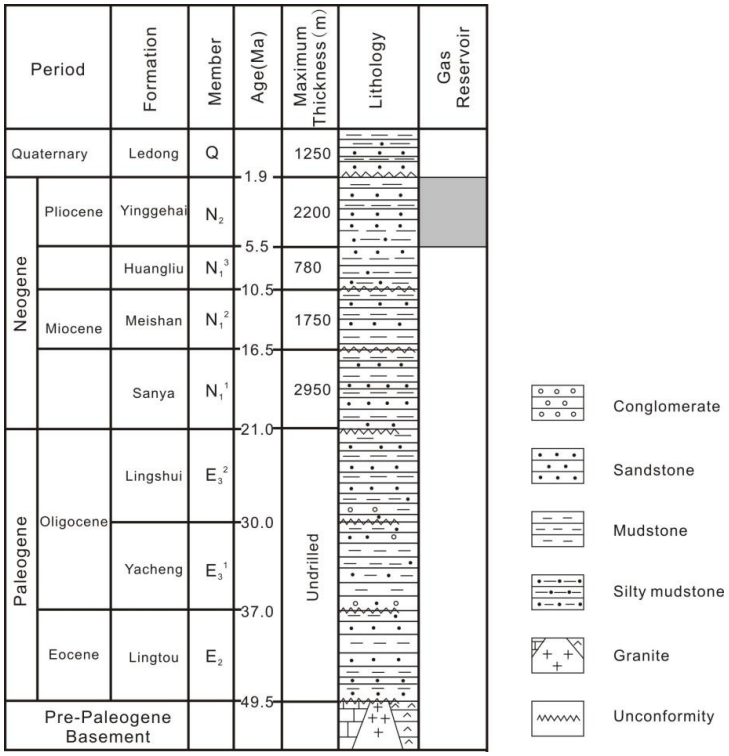

Figure 2. Simplified stratigraphic column of the Yinggehai basin modified after Gong et al. (1997) and Huang et al. (2003).

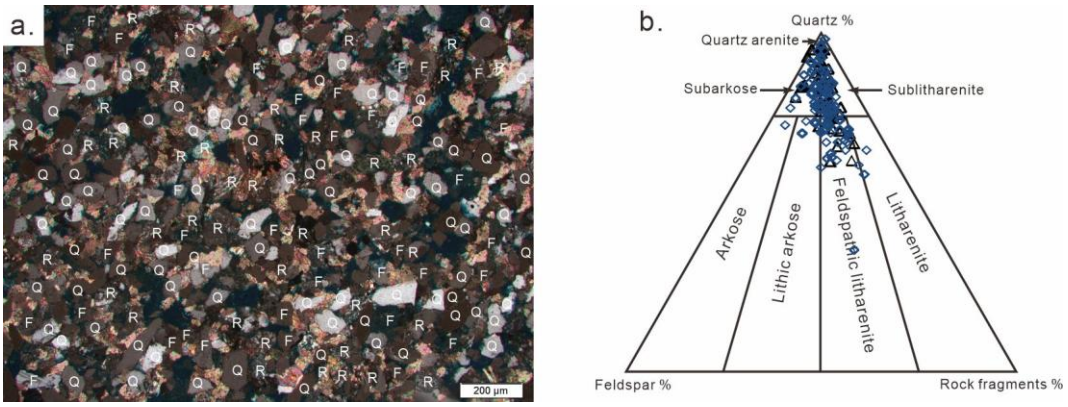

Figure 3. a) Image of a thin section of a sandstone sample collected from a depth of 1860.72 m in the LDX-1-1 well showing its detrital minerals: Q=quartz, F=feldspar and R=rock fragment. b) Mineral composition diagram, after Folk (1968), of the dawsonite-bearing samples from well LDX-1-1 (blue rhombuses) and well LDX-1-4 (black triangles). All the data were obtained through point-counting - see text.

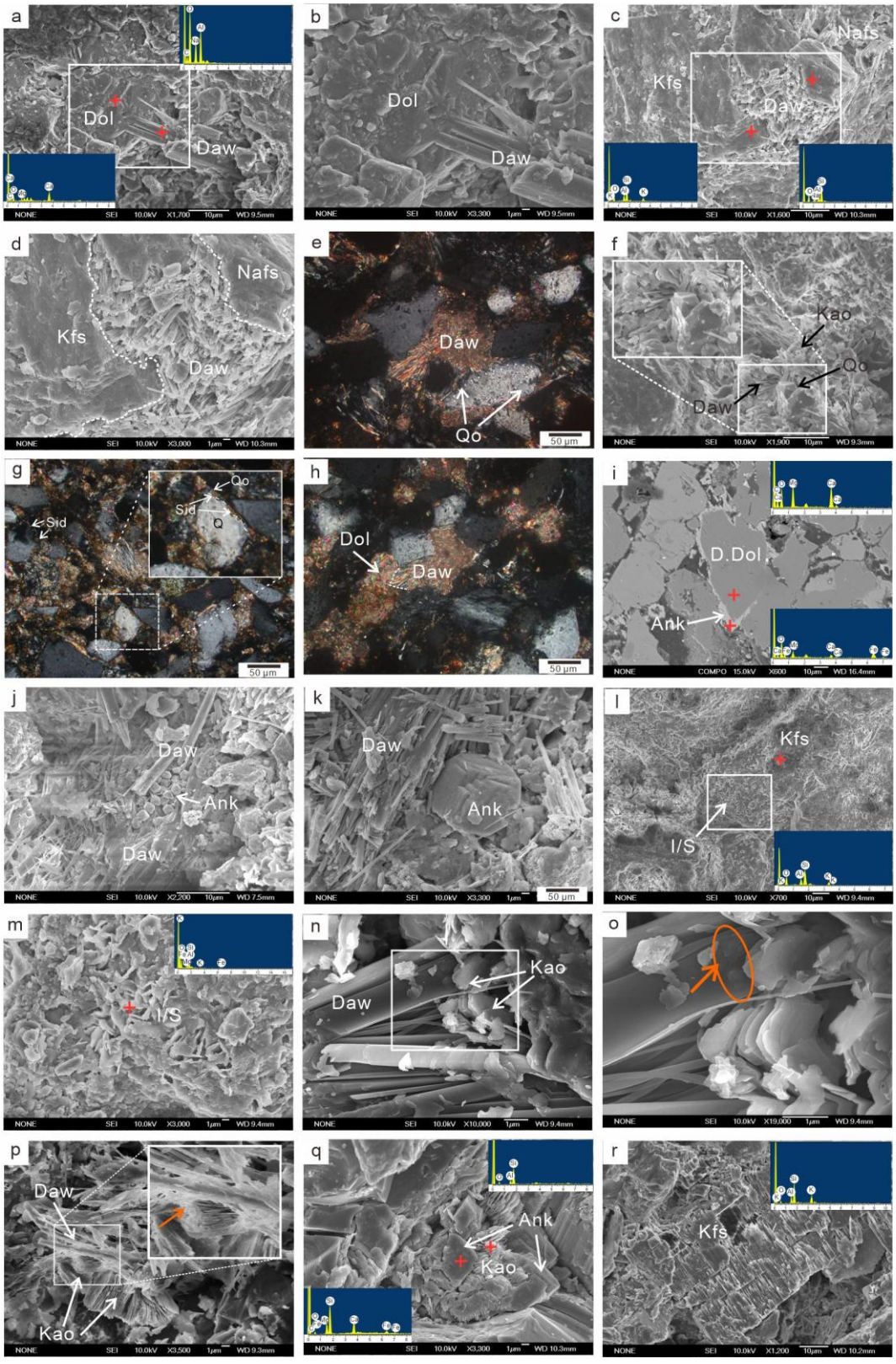

Figure 4. Micrographs of diagenetic minerals. (a, b) Acicular dawsonite growing on top of dolomite (red crosses are EDS probe spots), SEM; (c, d) Dawsonite replacing feldspar and plagioclase with EDS analysis results (red crosses are EDS probe spots); (e) Dawsonite replacing quartz overgrowths, thin section micrograph, cross polar; (f) Microcrystalline quartz grows with kaolinite on the top of drusy dawsonite, SEM; (g) Siderite surrounding detrital

minerals and on the inner side of quartz overgrowths, thin section micrograph, cross polar; (h) Dawsonite replacing dolomite (dashed line), thin section micrograph, cross polar; (i) Ankerite enclosing and replacing dolomite (red crosses are EDS probe spots), BSM; (j) rhombic-like ankerite with dawsonite in the pores, SEM; (k) the growth of rhombic-like ankerite adhering the dawsonite, SEM; (l, m) honeycombed-like illite and smectite mixed layer coating on detrital K-feldspar (red crosses are EDS probe spots), SEM; (n) kaolinite growing on drusy dawsonite, SEM; (o) Magnification of white box area in figure (n), some tiny etch pits are observed (red arrow, in the red circle) on dawsonite potentially caused by the growth of kaolinite, SEM; (p) Acicular dawsonite overlying (red crosses) kaolinite aggregation; (q) ankerite formed on the top of kaolinite aggregation (red crosses are EDS probe spots), SEM; (r) dissolution of K-feldspar and EDS results, SEM image. Qo: quartz overgrowth; Daw: dawsonite; Kao: kaolinite; Sid: siderite; Dol: dolomite; C: Detridal dolomite Ank: ankerite; I/S: illite and smectite mixed layer; Kfs: K-feldspar; Nafs: Na-feldspar.

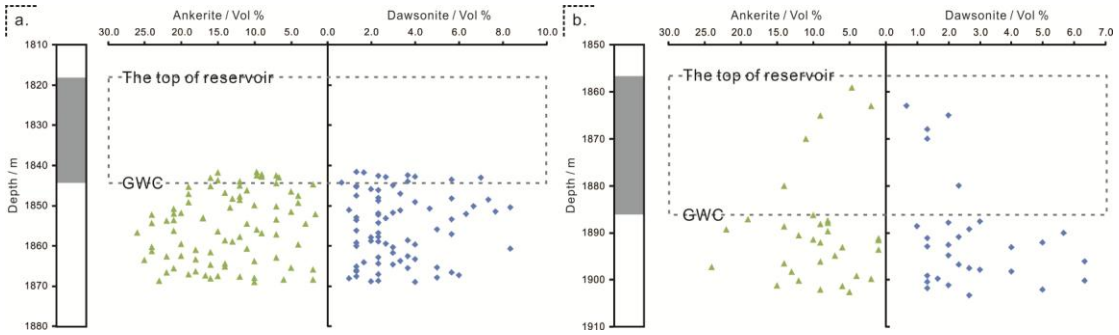

Figure 5. Plot of volume percent versus depth for dawsonite (blue rhombuses) and ankerite (green triangles) in well LDX-1-1 (Fig 3a) and well LDX-1-4 (Fig 3b). The filled gray areas and dashed boxes indicate the location of gas layers, the water layers in the reservoir system are below the gas layers. The gas-water-contact (GWC), as reported by the China National Offshore Oil Company are located at 1844.1m and 1886.0m depth in wells LDX-1-1 and LDX-1-4, respectively.

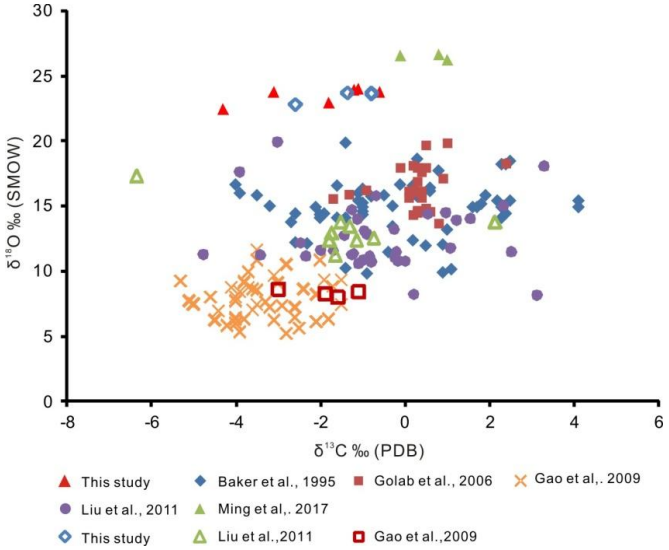

Figure 6. Plot of $\delta^{13}C$ versus $\delta^{18}O$ values for dawsonite and ankerite samples. Filled symbols represent the compositions of dawsonite, and open symbols for ankerite The filled red triangles and open blue rhombus correspond to compositions measured in this study from the LDX-1 structure, Yinggehai basin, China. Compositions of dawsonite from the Bowen-Gunnedah-Sydney basin system in Australia reported by Baker et al. (1995) are shown as filled blue rhombuses, those from the late Permian coal measures of the Upper Hunter Valley in Australia reported by Golab et al. (2006) are shown as filled dark red squares, those of the Cretaceous Hailaer basin in China reported by Gao et al. (2009) are shown as filled yellow crosses, those of the upper Cretaceous Songliao Basin in China reported by Liu et al. (2011) are shown as filled purple circles, and those of the Yaojie coalfield, Minhe basin in China reported by Ming et al. (2017) are shown as filled green triangles. Compositions of ankerite from the Cretaceous Hailaer basin in China reported by Gao et al. (2009) are shown as open red squares, and those of the upper Cretaceous Honggang anticline of the Songliao Basin in China reported by Liu et al. (2011) are shown as open green triangles.

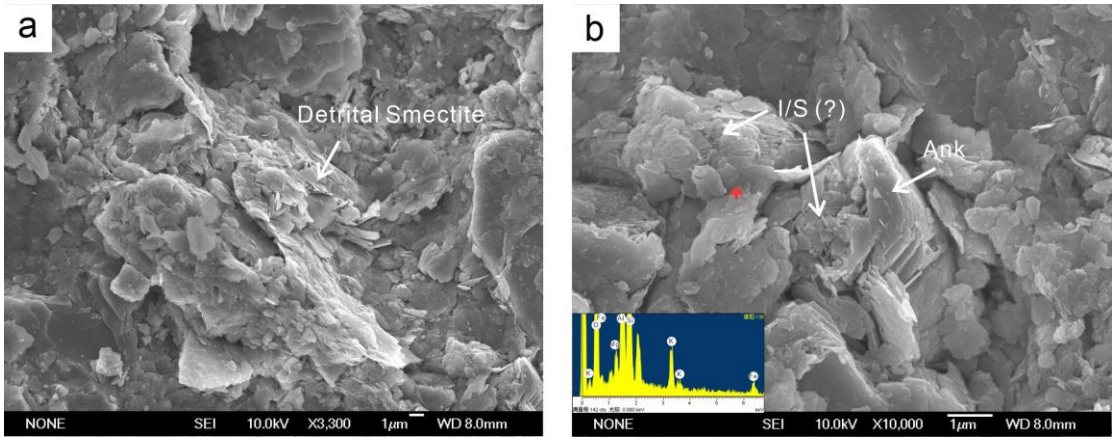

Figure 7. Images of clay minerals observed in this study. (a) detrital smectite in the sandstone and (b) image showing the relationship between smectite and ankerite. Rhombic ankerite crystals grew and adhered to the mixed layer of illite/smectite, suggesting the transformation of smectite could provide some of the materials for ankerite. I/S: mixed

layer of illite/smectite; Ank: ankerite.

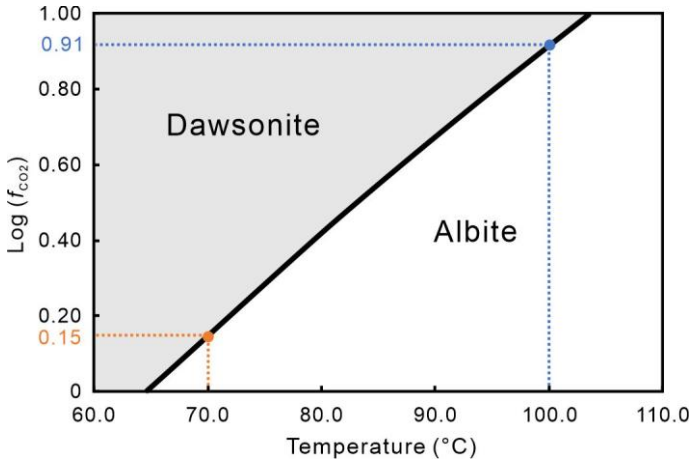

Figure 8 Log fugacity of CO_2 (log(f_{CO2})) versus temperature (°C) diagram depicting mineral stability fields in the system Na_2O-Al_2O_3-SiO_2-CO_2-H_2O balanced on Al and at quartz equilibrium. The grey area indicates the stability field of dawsonite, and the white area indicates the stability field for albite. The orange and blue lines highlight the log(f_{CO2}) values in equilibrium with dawsonite and albite at 70 and 100 °C, respectively. This figure was generated using PHREEQC together with its llnl database – see text.

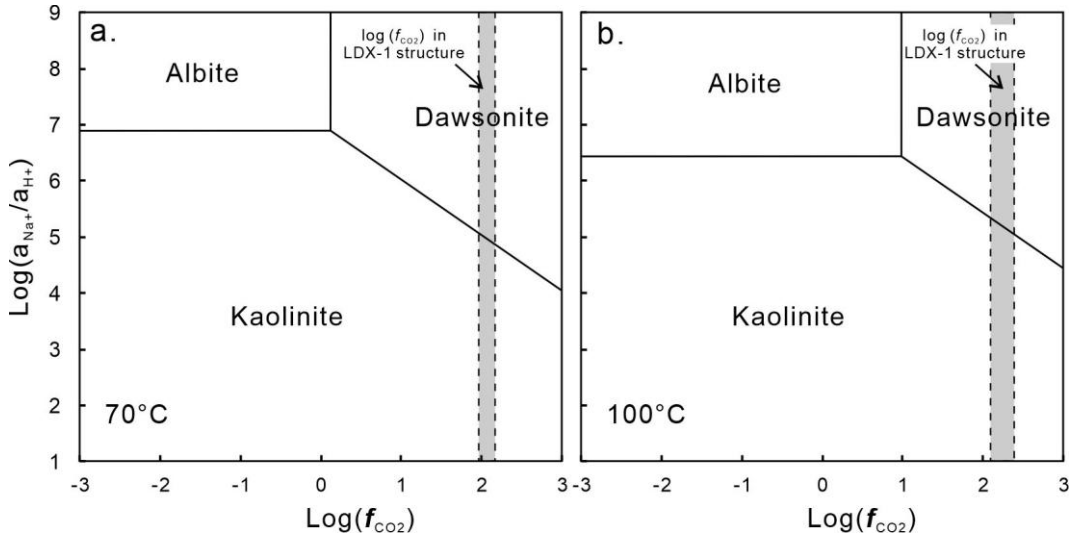

Figure 9. Log fugacity of CO_2 (log(f_{CO2})) versus log a_{Na+}/a_{H+} diagrams depicting mineral stability fields in the system Na_2O-Al_2O_3-SiO_2-CO_2-H_2O balanced on Al and at quartz equilibrium at 70 °C and 100 °C. The dashed area represents the current log (f_{CO2}) range in the reservoirs considered in this study. This figure was generated using PHREEQC together with its llnl database – see text.

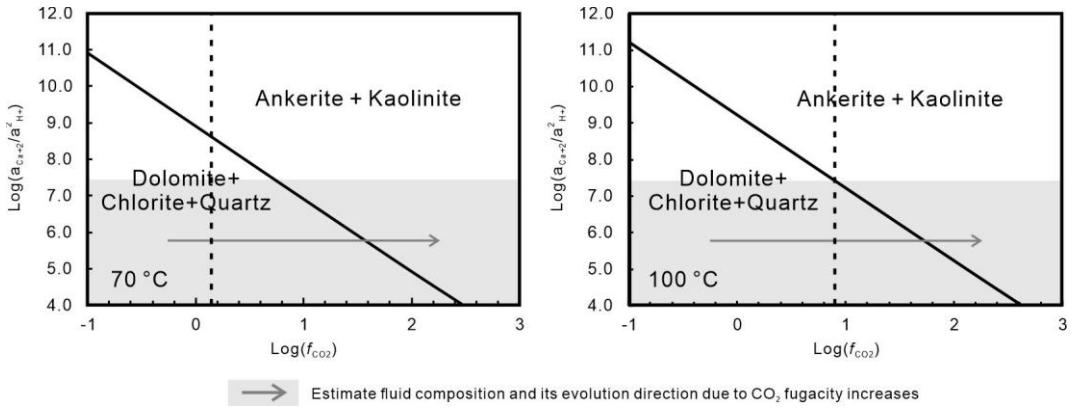

Figure 10. Phase diagram of log CO_2 fugacity (log (f_{CO2})) versus log a_{Ca2+}/a^2_{H+}. The dashed vertical lines correspond to equilibrium compositions of reaction 1, whereas the sloped lines correspond to equilibrium compositions of reaction 3, The grey area is the likely aqueous activity ratio of a_{Ca2+}/a^2_{H+} in the studied system and the arrow illustrates the direction of the CO_2 fugacity evolution in the system as the reservoir fills with CO_2. This figure was generated using PHREEQC together with its llnl database after adding estimated values for the thermodynamics properties of ankerite– see text.

924

925

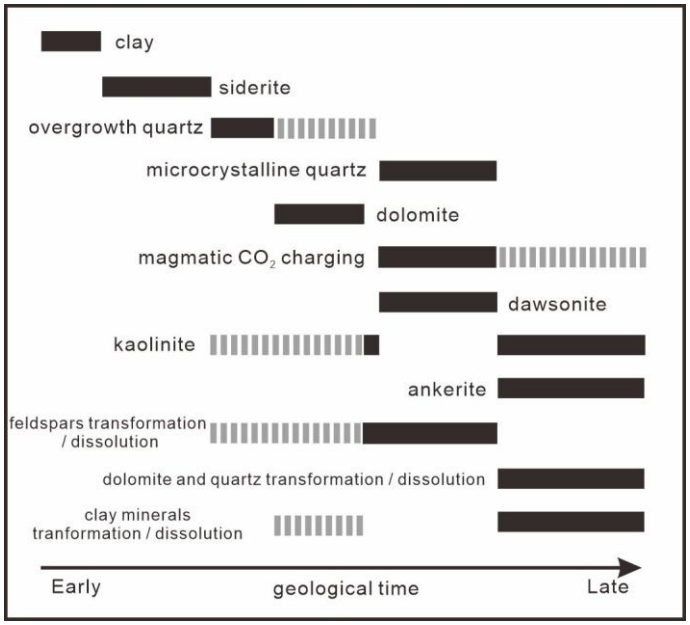

926

927 Figure 11. Paragenetic sequence for dawsonite-bearing sandstones in this study. The black bars are indicated by
928 petrologic observations, the grey dashed bars are estimated based on the mass balance considerations and reactions
929 (1) and (3).

930

931

932 **Table 1. EDS analysis data for dawsonite.**

Well	Weight Percentage, %					Atomic Percentage, %				
	C	Na	Al	O	Si	C	Na	Al	O	Si
LDX-1-1	18.76	4.98	12.99	63.27	n.d.	25.14	3.48	7.75	63.63	n.d.
LDX-1-1	15.88	11.13	14.19	58.8	n.d.	22.01	8.06	8.76	61.18	n.d.
LDX-1-1	11.81	12.44	12.96	55.55	7.23	17.14	9.44	8.38	60.55	4.49
LDX-1-4	14.88	13.8	14.24	57.09	n.d.	20.87	10.11	8.89	60.13	n.d.
LDX-1-4	15.61	12.53	13.7	58.15	n.d.	21.71	9.11	8.48	60.7	n.d.
LDX-1-4	12.62	14.69	17.98	54.72	n.d.	18.19	11.06	11.54	59.21	n.d.
LDX-1-4	12.64	8.37	14.29	57.5	7.2	18.15	6.28	9.14	62	4.43
LDX-1-4	7.83	6.83	8.83	55.28	21.23	11.88	5.41	5.96	62.97	13.78
LDX-1-4	12.58	12.01	19.97	55.44	n.d.	18.13	9.04	12.82	60.01	n.d.
LDX-1-4	9.14	14.68	24.74	51.45	n.d.	13.75	11.54	16.57	58.13	n.d.
LDX-1-1	10.16	13.06	23.91	52.87	n.d.	15.09	10.13	15.81	58.96	n.d.
LDX-1-1	11.59	9.4	23.75	55.26	n.d.	16.9	7.16	15.42	60.52	n.d.
LDX-1-1	18.76	4.98	12.99	63.27	n.d.	25.14	3.48	7.75	63.63	n.d.
LDX-1-1	11.97	10.19	18.04	55.91	3.88	17.36	7.72	11.64	60.86	2.41
LDX-1-1	7.25	12.06	30.26	50.43	n.d.	11.18	9.71	20.76	58.35	n.d.
LDX-1-1	13.42	13.99	16.92	55.67	n.d.	19.16	10.43	10.75	59.66	n.d.
LDX-1-1	13.68	13.29	16.93	56.11	n.d.	19.46	9.88	10.72	59.94	n.d.
LDX-1-1	18.6	7.9	11.21	62.28	n.d.	24.98	5.54	6.7	62.78	n.d.
LDX-1-1	12.75	11.24	20.18	55.83	n.d.	18.34	8.45	12.92	60.29	n.d.
LDX-1-1	10.17	12.49	24.3	53.04	n.d.	15.1	9.69	16.07	59.14	n.d.
LDX-1-4	13.71	7.2	12.99	58.84	7.26	19.43	5.33	8.2	62.63	4.4
LDX-1-4	11.98	13.11	16.51	55.02	3.38	17.39	9.93	10.66	59.92	2.1
LDX-1-4	10.86	13.85	21.98	53.31	n.d.	16	10.65	14.41	58.94	n.d.
LDX-1-4	22.23	3.58	7.27	66.93	n.d.	28.65	2.41	4.17	64.77	n.d.
LDX-1-4	10.18	12.73	24.1	52.99	n.d.	15.12	9.88	15.93	59.07	n.d.
LDX-1-4	12.26	13.58	19.45	54.7	n.d.	17.75	10.27	12.53	59.44	n.d.

933 **n.d.: not be detected.**

934

935 **Table 2. EDS analysis data for ankerite**

Well	Weight Percent								Atomic Percent							
	C	O	Na	Mg	Al	Si	Ca	Fe	C	O	Na	Mg	Al	Si	Ca	Fe
LDX-1-4	9.66	51.32	n.d.	6.54	n.d.	4.42	6.29	21.77	16.14	64.34	n.d.	5.4	n.d.	3.16	3.15	7.82
LDX-1-4	13.15	52.72	n.d.	8.46	n.d.	n.d.	19.73	5.95	20.52	61.75	n.d.	6.52	n.d.	n.d.	9.22	2
LDX-1-4	10.3	53.98	n.d.	7.09	n.d.	1.77	17.26	9.6	16.53	65.02	n.d.	5.62	n.d.	1.22	8.3	3.31
LDX-1-4	12.96	57.98	n.d.	5.16	2.28	1.72	1.12	18.77	19.89	66.79	n.d.	3.92	1.56	1.13	0.52	6.2
LDX-1-4	16.52	61.57	n.d.	7.64	n.d.	n.d.	0.92	13.35	23.71	66.35	n.d.	5.42	n.d.	n.d.	0.39	4.12
LDX-1-4	12.79	61.42	n.d.	6.25	1.52	2.56	2.73	12.73	19	68.49	n.d.	4.59	1	1.62	1.21	4.07
LDX-1-4	15.63	55.85	n.d.	3.64	1.34	4.16	11.59	7.79	23.37	62.69	n.d.	2.69	0.89	2.66	5.19	2.5
LDX-1-1	13.97	59.87	1.84	5.04	1.69	0.84	12.09	4.66	20.51	66	1.41	3.66	1.1	0.53	5.32	1.47
LDX-1-1	13.39	59.42	n.d.	5.56	n.d.	2.16	12.7	6.78	20.01	66.65	n.d.	4.1	n.d	1.38	5.69	2.18
LDX-1-1	12.41	60.07	n.d.	3.29	2.27	11.6	3.16	7.2	18.36	66.71	n.d.	2.4	1.49	7.34	1.4	2.29
LDX-1-1	10.25	45.23	n.d.	3.86	2.24	5.18	16.05	17.17	17.73	58.71	n.d.	3.3	1.73	3.83	8.32	6.39

936 **n.d.: not be detected.**

937

938 **Table 3. EDS analysis data for smectite and the mixed layer of illite and smectite**

Well	Weight Percentage, %									Atomic Percentage, %								
	C	O	Na	Mg	Al	Si	K	Ca	Fe	C	O	Na	Mg	Al	Si	K	Ca	Fe
LDX-1-1	3.31	57	2.64	0.63	6.64	26.9	1.24	0.37	1.27	5.25	67.91	2.19	0.49	4.69	18.26	0.6	0.18	0.43
LDX-1-1	n.d.	41.41	n.d.	1.22	9.69	35.81	6.72	n.d.	5.14	n.d.	57.05	n.d.	1.11	7.92	28.11	3.79	n.d.	2.03
LDX-1-1	n.d.	37.5	n.d.	1.55	9.06	39.51	4.7	n.d.	7.67	n.d.	53.18	n.d.	1.44	7.62	31.92	2.73	n.d.	3.12
LDX-1-1	n.d.	47.11	1.39	1.93	14.08	26.38	2.12	n.d.	6.99	n.d.	62.32	1.28	1.68	11.04	19.88	1.15	n.d.	2.65
LDX-1-4	n.d.	57.17	0.7	0.99	15.27	22.26	2.53	n.d.	1.08	n.d.	70.24	0.6	0.8	11.13	15.58	1.27	n.d.	0.38
LDX-1-4	n.d.	54.36	n.d.	4.31	8.23	11.71	n.d.	13.46	7.93	n.d.	71.16	n.d.	3.71	6.38	8.73	n.d	7.03	2.98
LDX-1-4	n.d.	52.97	n.d.	1.18	13.35	26.82	4.82	n.d.	0.87	n.d.	66.92	n.d.	0.98	10	19.3	2.49	n.d.	0.31
LDX-1-4	n.d.	55.21	n.d.	1.52	11.51	27.18	1.39	n.d.	3.18	n.d.	69.01	n.d.	1.25	8.53	19.35	0.71	n.d.	1.14
LDX-1-4	n.d.	45.84	n.d.	1.44	14.38	28.31	3.13	n.d.	6.91	n.d.	61.37	n.d.	1.27	11.42	21.59	1.71	n.d.	2.65
LDX-1-4	n.d.	46.01	n.d.	1.67	12.96	29.18	2.94	n.d.	7.24	n.d.	61.6	n.d.	1.47	10.29	22.25	1.61	n.d.	2.78
LDX-1-4	n.d.	46.45	n.d.	1.52	15.13	26.85	4.9	n.d.	5.16	n.d.	61.77	n.d.	1.33	11.93	20.34	2.67	n.d.	1.96
LDX-1-4	n.d.	52.5	n.d.	1.34	13.43	26.4	2.83	n.d.	3.49	n.d.	66.84	n.d.	1.12	10.14	19.15	1.48	n.d.	1.27
LDX-1-4	n.d.	52.32	1.04	1.26	9.4	29.16	1.99	n.d.	3.28	n.d.	66.71	0.92	1.05	7.11	21.18	1.04	0.79	1.2
LDX-1-4	n.d.	39.97	n.d.	1.14	10.55	39.83	2.53	n.d.	4.37	n.d.	55.06	n.d.	1.04	8.62	31.26	1.43	0.87	1.73
LDX-1-4	n.d.	32.01	n.d.	0.97	12.81	34.05	12.63	n.d.	7.54	n.d.	47.8	n.d.	0.95	11.34	28.97	7.72	n.d.	3.23
LDX-1-4	n.d.	53.67	0.98	0.99	11.99	28.2	2.38	n.d.	1.8	n.d.	67.37	0.86	0.82	8.92	20.16	1.22	n.d.	0.65
LDX-1-1	n.d.	53.91	n.d.	1.68	12.75	25.32	4.2	n.d.	2.13	n.d.	67.96	n.d.	1.4	9.53	18.18	2.17	n.d.	0.77
LDX-1-1	n.d.	61.56	1.25	0.99	9.68	22.71	2.14	n.d.	1.68	n.d.	74.07	1.04	0.79	6.9	15.56	1.05	n.d.	0.58
LDX-1-1	n.d.	63.93	1.67	2.62	8.94	16.76	1.11	n.d.	4.97	n.d.	76.52	1.39	2.06	6.35	11.43	0.54	n.d.	1.7
LDX-1-1	n.d.	35.98	n.d.	1.82	11.82	35.41	8.01	n.d.	6.96	n.d.	51.68	n.d.	1.72	10.07	28.97	4.7	n.d.	2.86

939 **n.d.: not be detected.**

940
941

Table 4. Carbon and oxygen isotopic compositions for dawsonite and ankerite

Well	Depth	Mineral	$\delta^{13}C$	$\delta^{18}O$	$\delta^{18}O$	Isotopic temp.	$\delta^{13}C_{CO2}$
	m		‰, PDB	‰, PDB	‰, SMOW	ºC	‰, PDB
LDX-1-4	1894.8	Dawsonite	-1.2	-6.8	23.9	68.53	-7.39
LDX-1-4	1896.07	Dawsonite	-1.1	-6.7	24.0	67.83	-7.34
LDX-1-4	1897.57	Dawsonite	-0.6	-7.0	23.7	69.94	-6.69
LDX-1-4	1900.2	Dawsonite	-1.8	-7.8	22.9	75.76	-7.44
LDX-1-1	1842.5	Dawsonite	-4.3	-8.3	22.4	79.56	-9.66
LDX-1-1	1863.34	Dawsonite	-3.1	-7.0	23.7	69.94	-9.17
LDX-1-4	1889.07	Ankerite	-2.6	-7.8	22.8	96.44	-7.27
LDX-1-4	1894.8	Ankerite	-0.8	-7.0	23.7	89.56	-5.94
LDX-1-4	1897.57	Ankerite	-0.8	-7.1	23.6	90.31	-5.88
LDX-1-4	1900.2	Ankerite	-1.4	-7.0	23.7	89.56	-6.50

942